

# How to administer an antidote to Schrödinger’s cat

Juan-Rafael Álvarez,<sup>1</sup> Mark IJspeert,<sup>1</sup> Oliver Barter,<sup>1</sup> Ben Yuen,<sup>1,\*</sup> Thomas D. Barrett,<sup>1,†</sup> Dustin Stuart,<sup>1</sup> Jerome Dilley,<sup>1,‡</sup> Annemarie Holleccek,<sup>1,§</sup> and Axel Kuhn<sup>1,¶</sup>

<sup>1</sup>*University of Oxford, Clarendon Laboratory, Parks Road, Oxford OX1 3PU, UK*

(Dated: June 18, 2021)

In his 1935 Gedankenexperiment, Erwin Schrödinger imagined a poisonous substance which has a 50% probability of being released, based on the decay of a radioactive atom. As such, the life of the cat and the state of the poison become entangled, and the fate of the cat is determined upon opening the box. We present an experimental technique that keeps the cat alive on any account. This method relies on the time-resolved Hong-Ou-Mandel effect: two long, identical photons impinging on a beam splitter always bunch in either of the outputs. Interpreting the first photon detection as the state of the poison, the second photon is identified as the state of the cat. Even after the collapse of the first photon’s state, we show their fates are intertwined through quantum interference. We demonstrate this by a sudden phase change between the inputs, administered conditionally on the outcome of the first detection, which steers the second photon to a pre-defined output and ensures that the cat is always observed alive.

## I. INTRODUCTION

One of the most intriguing principles of quantum mechanics is that of superposition, which states that a quantum system, before being measured, can be interpreted to be in two simultaneous states at once. In his 1935 Gedankenexperiment [1], Erwin Schrödinger illustrated the paradoxical nature of superposition by depicting a cat in a box whose state (dead or alive) is entangled with a vicious device releasing a poisonous substance upon a 50% probable radioactive decay. Only upon opening the box for the first time, is it possible to determine the state of the combined system of the cat and the radioactive device; with no decay together with an intact vile and a cat observed alive only half of the time.

The randomness of quantum measurements introduces a fundamental distinction with respect to classical measurements. The process of measurement is central to many open theoretical questions [2], where the measurement induces apparent contradictions between the predictions of quantum mechanics and the appearance of sharp measurement outcomes [3]. In addition, many systems and applications involve a form of quantum control that relies on the quantum nature of measurements [4].

This poses the question: can a partial measurement of a quantum system be made such that it triggers a sequence of events that coerces the remainder of the system

into a desired state? In the example of Schrödinger’s cat, such an ability would ensure that the cat is always observed alive, whether or not the poison has been released. Such an approach would normally be implemented in the form of a feedback loop, by which a device obtains information about the trajectory of a physical system in order to modify it in real time [5, 6].

In quantum systems, feedback can be of two types: the first, measurement-based quantum feedback, occurs when a measurement outcome defines a subsequent action on the original system. The second, coherent quantum feedback, involves no measurements but provides control using coherent interaction with an auxiliary quantum system.

Both feedback types exist in a range of applications: the generation of amplitude squeezed states in a semiconductor laser [7], the improvement of single-shot phase measurements in quantum metrology [8], the stabilisation of a combined atom-cavity quantum state [9], and the preparation and stabilisation of Fock states in a high-Q microwave cavity with weak measurements [10, 11].

In this work, we take advantage of a measurement-based feedback protocol to deliver a photonic state with a desired property: that of always exiting through the output of a beam splitter of the experimentalist’s choosing. Specifically, the feedback process is applied in a time-resolved two-photon quantum interference experiment [12] in which the time span between the first and second photon detection is long enough ( $\sim 500$  ns) for a phase change to be applied on the second photon. This allows us to alternate between the behaviours of bosonic and fermionic interference to control the routing of a single photon as desired.

---

\*now at Metamaterials Research Centre, University of Birmingham, Edgbaston, Birmingham, B15 2TT, UK

†now at InstaDeep, London, UK.

‡now at Google.

§now at Robert Bosch GmbH, Postfach 13 55, 74003 Heilbronn, Germany

¶Electronic address: axel.kuhn@physics.ox.ac.uk

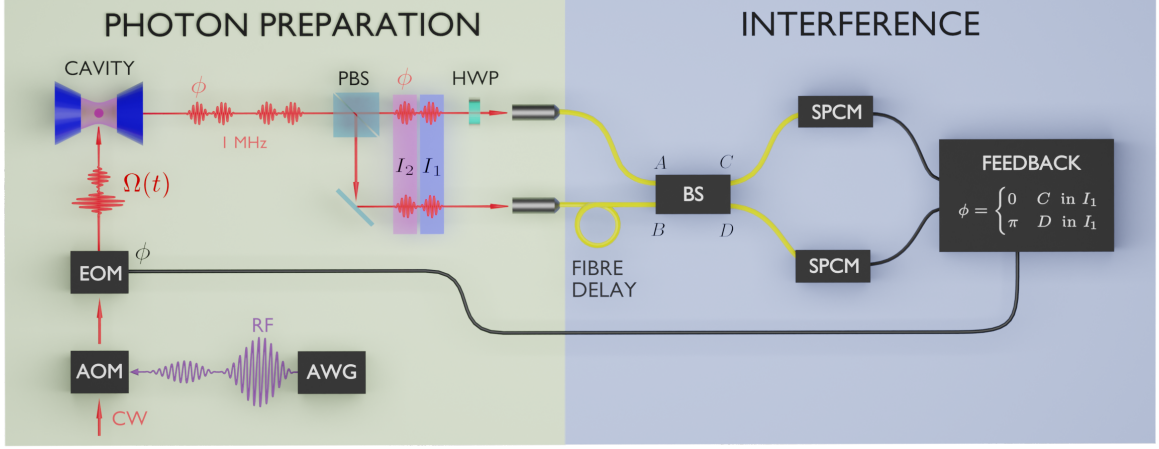


FIG. 1: Experimental arrangement: Two long, double-hump photons interfere in a beam splitter. Photons are emitted at a repetition rate of 1 MHz from an atomic source driven by a laser pulse controlled by an acousto-optic modulator (AOM), whose phase is changed using an electro-optic modulator (EOM). The AOM pulses are generated by an arbitrary waveform generator (AWG). A delay line with an optical path length of 300 m ensures the simultaneous arrival of two sequentially emitted photons. The emitted photons have such long wave packets, that the first time bin of both photons interferes before the relative phase  $\phi$  of the second photon in the second time bin is set. Furthermore, the emitted photons have random polarisations. Using a polarising beam splitter (PBS), photons are routed into random paths, and two photons simultaneously impinge on the input ports  $A$  and  $B$  of a beam splitter (BS) in 25% of all possible cases. The relative polarisation between both photons is changed using a half wave plate (HWP). Photons then interfere in the BS and exit through the ports  $C$  and  $D$ , upon which measurements are performed using single photon counting modules (SPCMs). The outcome of a measurement in the first time bin is used to perform feedback on the value of the phase,  $\phi$  during the second half of the driving pulse.

## II. THEORY

Let us consider two photons arriving simultaneously at the input ports  $A$  and  $B$  of a beam splitter (BS), as illustrated in the Interference box of Fig. 1. The joint probability of detecting two photons at times  $t_0$  and  $t_0 + \tau$  at detectors placed at outputs  $C$  and  $D$  of the BS, respectively, can be written as [12, 13]

$$P_{\text{joint}}(t_0, \tau) = \left| \hat{E}_D^+(t_0 + \tau) \hat{E}_C^+(t_0) \hat{a}_A^\dagger \hat{a}_B^\dagger |0_A 0_B\rangle \right|^2, \quad (1)$$

where  $\hat{a}_A^\dagger$  and  $\hat{a}_B^\dagger$  correspond to the creation operators of a photon in the ports  $A$  and  $B$  ( $\hat{a}_A$  and  $\hat{a}_B$  would correspond to the annihilation operators),  $\hat{E}_C^+ + \hat{E}_D^+$  and  $\hat{E}_D^+ + \hat{E}_C^+$  are the electric field operators at the output ports of the beam splitter, and  $|0_A 0_B\rangle$  corresponds to the vacuum state on the input ports  $A$  and  $B$ . In this context,  $\tau$  can be positive or negative, and  $\tau < 0$  corresponds to the detector in port  $D$  clicking before that in port  $C$ . We emphasise that  $\tau$  is a detection time difference giving rise to a time-resolved Hong-Ou-Mandel (HOM) signal [12, 13], and must not be confused with the photon arrival time difference ( $\Delta t$ ) used in many other HOM experiments [14]. Here, we are only interested in the case for which the two photon wavepackets arrive simultaneously ( $\Delta t = 0$ ).

The electric field operators can be written as the sum of spatio-temporal functions in distinct modes  $k$ ,  $\zeta_k(t) =$

$$\epsilon_k(t) \exp(-i\phi_k(t)):$$

$$\hat{E}^+(t) = \sum_k \zeta_k(t) \hat{a}_k, \quad \hat{E}^-(t) = \sum_k \zeta_k^*(t) \hat{a}_k^\dagger, \quad (2)$$

where  $\epsilon_k(t)$  corresponds to the photon amplitude in mode  $k$  and  $\phi_k(t)$  to its phase.

Since the absolute photon detection times are irrelevant, we calculate the joint detection probability as a function of  $\tau$  only:

$$P_{\text{joint}}(\tau) = \int_{-\infty}^{\infty} dt_0 P_{\text{joint}}(t_0, \tau). \quad (3)$$

For two linearly polarised photons with a relative polarisation angle  $\theta$ , Eq. 1 can be written as [13]

$$P_{\text{joint}}(t_0, \tau) = P_{\text{joint}}^{(HV)}(t_0, \tau) - \cos^2 \theta F(t_0, \tau), \quad (4)$$

where

$$P_{\text{joint}}^{(HV)}(t_0, \tau) = \frac{1}{4} \left( |\epsilon_A(t_0) \epsilon_B(t_0 + \tau)|^2 + |\epsilon_A(t_0 + \tau) \epsilon_B(t_0)|^2 \right) \quad (5)$$

and

$$F(t_0, \tau) = \frac{\epsilon_A(t_0) \epsilon_B(t_0 + \tau) \epsilon_A(t_0 + \tau) \epsilon_B(t_0)}{2} \times \cos(\phi_A(t_0) - \phi_A(t_0 + \tau) + \phi_B(t_0 + \tau) - \phi_B(t_0)). \quad (6)$$

When both input photons have orthogonal polarisations ( $\theta = \pi/2$ ),  $P_{\text{joint}}(\tau)$  can be written as the convolution of their spatio-temporal squared amplitudes,  $P_{\text{joint}}(\tau) = \frac{1}{2} \left( |\varepsilon_A|^2 * |\varepsilon_B|^2 \right)(\tau)$ , rendering the choice of  $\phi_A$  and  $\phi_B$  irrelevant. This is in sharp contrast to the case for which both input photons have parallel polarisations ( $\theta = 0$ ), where  $\phi_A$  and  $\phi_B$  become relevant. The expected behaviour of  $P_{\text{joint}}(\tau)$  for the particular case of two photons of perpendicular polarisation with the temporal shape  $\epsilon(t) = \sin^2(2\pi t/\delta t)$ , is shown as a dashed curve in Fig. 3(a) for  $\delta t = 401$  ns. The three peaks that are shown in Fig. 3(a) correspond to the detection of coincidences in detectors  $C$  and  $D$  delayed by varying time differences  $\tau \in [-401, 401]$  ns.

We subdivide the overall duration of the photons into two distinct intervals (bins) of equal length labeled  $I_1$  (early) and  $I_2$  (late). Additionally, let us assume that, for the photon arriving through  $A$ ,  $\phi_A(t) = 0$  for all times, and that, for the photon arriving through  $B$ ,  $\phi_B(t) = 0$  for  $t \in I_1$ , and  $\phi_B(t) = \phi$  for  $t \in I_2$ . In the Schrödinger picture [13], the state entering the BS is given by

$$|\Psi_{\text{in}}\rangle = \frac{1}{2} \left( \hat{a}_{A1}^\dagger + \hat{a}_{A2}^\dagger \right) \left( \hat{a}_{B1}^\dagger + e^{i\phi} \hat{a}_{B2}^\dagger \right) |0\rangle. \quad (7)$$

Here,  $\hat{a}_{Aj}^\dagger$  and  $\hat{a}_{Bj}^\dagger$  correspond to the photon creation operators in ports  $A$  and  $B$  in the time intervals  $I_j$ , with  $j \in \{1, 2\}$ , and  $|0\rangle$  is the vacuum state in the basis of all the temporal and beam splitter input paths:  $|0\rangle = |0_{A1}0_{A2}0_{B1}0_{B2}\rangle$ . For the cases  $\phi = 0$  and  $\phi = \pi$ , the theoretical predictions of  $P_{\text{joint}}(\tau)$  are shown as dashed curves in Figs. 3(b) and (c). For the case of Fig. 3(b), both input photons are identical and feature photon bunching in the output detectors. For this reason, the expected behaviour would not include any coincidences between detectors  $C$  and  $D$ . In contrast, in Fig. 3(c) the photon entering through port  $B$  acquired a  $\pi$ -phase change from  $I_1$  to  $I_2$ . This is the only difference between the two photons. Therefore, if both photons are detected during either  $I_1$  or  $I_2$ , the photons are indistinguishable and no correlations are found with  $\tau \simeq 0$ . However, if the photons are detected in different intervals, the change in phase drives them to different outputs, resulting in a coincidence probability that is twice as large as the orthogonal polarisation case for  $\tau = \pm 201$  ns.

Figs. 3(b) and (c) exhibit a form that corresponds to a different type of interference between the two photons depending on the value of  $\phi$ . Bosonic ( $\phi = 0$ ) and fermionic interference ( $\phi = \pi$ ) is found with photons either bunching in the same outputs or avoiding each other and giving rise to coincidences, respectively. To see this, consider the following argument, using the Schrödinger picture: the operators after the beam splitter in the output channels  $C$  and  $D$  in  $I_j$  are linked to those before it by the standard unitary relation  $\hat{a}_{Aj,Bj}^\dagger = (\hat{a}_{Cj}^\dagger \pm \hat{a}_{Dj}^\dagger)/\sqrt{2}$ .

Therefore, after the beam splitter, Eq. 7 results in:

$$\begin{aligned} |\Psi_{\text{out}}\rangle = \frac{1}{2\sqrt{2}} & \left( \left( \hat{a}_{C1}^\dagger \hat{a}_{C1}^\dagger + e^{i\phi} \hat{a}_{C2}^\dagger \hat{a}_{C2}^\dagger \right. \right. \\ & \left. \left. - \hat{a}_{D1}^\dagger \hat{a}_{D1}^\dagger - e^{i\phi} \hat{a}_{D2}^\dagger \hat{a}_{D2}^\dagger \right) \right. \\ & + (e^{i\phi} + 1) \left( \hat{a}_{C1}^\dagger \hat{a}_{C2}^\dagger - \hat{a}_{D1}^\dagger \hat{a}_{D2}^\dagger \right) \\ & \left. + (e^{i\phi} - 1) \left( \hat{a}_{C2}^\dagger \hat{a}_{D1}^\dagger - \hat{a}_{C1}^\dagger \hat{a}_{D2}^\dagger \right) \right) |0\rangle. \quad (8) \end{aligned}$$

Here,  $|0\rangle$  is represented in the basis of all the output ports and temporal modes:  $|0\rangle = |0_{C1}0_{C2}0_{D1}0_{D2}\rangle$ . The first four terms account for both photons arriving at the same detector in the same time bin. These terms lead to the standard boson bunching reported in the canonical HOM effect [14]. The last four terms correspond to cross-correlations between detectors and/or time bins. Unless the single photon detectors are number resolving, it is not possible to measure outcomes where both detections occur at the same detector in the same time bin. By eliminating the terms of the form  $\hat{a}_{Xi}^\dagger \hat{a}_{Xi}^\dagger$  and rearranging the terms, the observable sub-state from Eq. 8 becomes

$$\begin{aligned} |\tilde{\Psi}_{\text{out}}\rangle = \frac{1}{2\sqrt{2}} & \left( \hat{a}_{C1}^\dagger \left( (e^{i\phi} + 1) \hat{a}_{C2}^\dagger - (e^{i\phi} - 1) \hat{a}_{D2}^\dagger \right) \right. \\ & \left. + \hat{a}_{D1}^\dagger \left( (e^{i\phi} - 1) \hat{a}_{C2}^\dagger - (e^{i\phi} + 1) \hat{a}_{D2}^\dagger \right) \right) |0\rangle. \quad (9) \end{aligned}$$

In this sub-state, the phase appears explicitly. By setting  $\phi = 0$ , Eq. 9 reads

$$|\tilde{\Psi}_{\text{out}}^{(\phi=0)}\rangle = \frac{1}{\sqrt{2}} \left( \hat{a}_{C1}^\dagger \hat{a}_{C2}^\dagger - \hat{a}_{D1}^\dagger \hat{a}_{D2}^\dagger \right) |0\rangle. \quad (10)$$

This state again leads to the canonical HOM effect, yet across the time bins this time. Therefore, both photons arrive at in the same detector, but in separate time intervals. In contrast, setting  $\phi = \pi$ , Eq. 9 now gives

$$|\tilde{\Psi}_{\text{out}}^{(\phi=\pi)}\rangle = \frac{1}{2\sqrt{2}} \left( \hat{a}_{C1}^\dagger \hat{a}_{D2}^\dagger - \hat{a}_{C2}^\dagger \hat{a}_{D1}^\dagger \right) |0\rangle, \quad (11)$$

which is strikingly different to Eq. 10, as both photons exhibit fermionic behaviour by arriving at different detectors.

Switching between the bosonic and fermionic behaviour by choice of  $\phi$  allows one to put the system into a pre-defined quantum state conditioned on the random outcome of the first measurement. This is implemented in the form of a feedback mechanism, where a photon detection at either detector in  $I_1$  reveals the required change of  $\phi$  to steer the remaining photon in  $I_2$  to a specific detector. For instance, if detector  $D$  clicks in  $I_1$ , the second detection would normally occur in detector  $D$ , due to the canonical HOM effect. However, as the second

halves of the photons have not reached the input ports at the moment of detection, we can instantly change the phase between  $I_1$  and  $I_2$  for one of the incoming photons to change the port in which the second detection occurs. By choosing  $\phi = \pi$  and projecting the output state in Eq. 11 onto the measured state  $|0_{C1}1_{D1}\rangle = \hat{a}_{D1}^\dagger |0_{C1}0_{D1}\rangle$  (involving only the first time bin, since the second one has not yet occurred), the state reduces to

$$\left\langle 0_{C1}0_{D1} \left| \hat{a}_{D1} \right| \tilde{\Psi}_{\text{out}}^{(\phi=\pi)} \right\rangle = \frac{1}{\sqrt{2}} \hat{a}_{C2}^\dagger |0_{C2}0_{D2}\rangle. \quad (12)$$

This state clearly shows that, when a measurement occurs in  $I_2$ , any click will be recorded in detector  $C$ . Analogously, if detector  $C$  clicks in  $I_1$  and  $\phi = 0$  is chosen, both photons are identical in their two halves and any detection in  $I_2$  will always occur at detector  $C$ . This reduces the quantum state to

$$\left\langle 0_{C1}0_{D1} \left| \hat{a}_{C1} \right| \tilde{\Psi}_{\text{out}}^{(\phi=0)} \right\rangle = \frac{1}{\sqrt{2}} \hat{a}_{C2}^\dagger |0_{C2}0_{D2}\rangle. \quad (13)$$

Again, when a measurement occurs in  $I_2$ , any click will be recorded by detector  $C$ . Eqs. 12 and 13 imply that  $\phi$  can be used as a parameter for feedback control, to steer the remaining photon to a desired output.

Returning to Eqs. (3) and (4) with a value of  $\phi$  conditional on the measurement of a photon in  $I_1$ , we observe the expected behaviour of  $P_{\text{joint}}(\tau)$ , as illustrated in Fig. 3(d). Fig. 3(d) shows increased coincidences with  $\tau < 0$ , for which a detection in  $D$  occurs before a detection in  $C$ . There are significantly less coincidences with  $\tau > 0$ , as this would correspond to detector  $C$  firing first and detector  $D$  second, which cannot occur with an active feedback that always prompts the second detection in  $C$ . Fig. 3 shows the subset of probabilities for cross-detector correlations only. For this reason, the value  $\int P_{\text{joint}}(\tau) d\tau$  is bounded by  $1/2$ . The theoretical curves for same-detector correlations are shown in the Supplementary Material.

### III. EXPERIMENTAL METHODS

To demonstrate this phenomenon experimentally, we generate photons in an atom-cavity system using a standard V-STIRAP scheme [15] coupling the hyperfine levels of the  $D_2$  line of  $^{87}\text{Rb}$ . Specifically, the  $|e\rangle = |5^2S_{1/2}, F=1\rangle$  and  $|g\rangle = |5^2S_{1/2}, F=2\rangle$  ground states are coupled in a  $\Lambda$ -scheme to the excited state  $|x\rangle = |5^2P_{3/2}, F'=3\rangle$  using a driving laser  $\Omega(t)$ , as illustrated in Fig. 2. The cavity has a decay rate of  $\kappa = 2\pi \times 12$  MHz and a maximum coupling strength of  $g_0 = 2\pi \times 15$  MHz. With the system initially prepared in  $|e, 0\rangle$ , the laser adiabatically drives the system to  $|g, 1\rangle$ , whereupon the

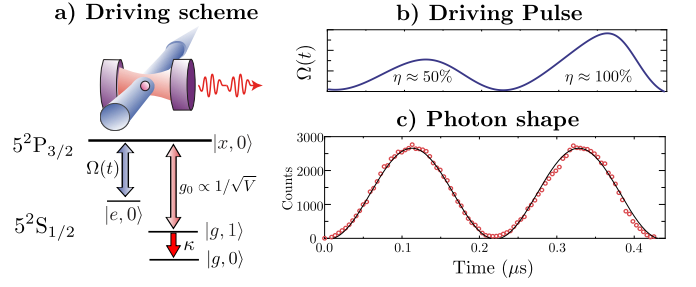


FIG. 2: Photon production scheme for the generation of double-hump photons. Fig (a) shows the driving scheme used to generate single photons for a single  $^{87}\text{Rb}$  atom inside of an optical cavity, following a coherent STIRAP process between the  $|F=1\rangle \equiv |e\rangle$  and  $|F=2\rangle \equiv |g\rangle$  ground states of  $^{87}\text{Rb}$  via the virtually excited state  $|F'=3\rangle \equiv |x\rangle$  [16]. (b) shows the pre-calculated [17] pulse necessary for the photon shape to follow the form  $\sin^2(2\pi\tau)$  with  $0 < \tau < 1$ , where  $\tau = t/450$  ns, as can be seen theoretically (solid line) and experimentally (dots) in (c). Our cavity has a decay rate of  $\kappa = 2\pi \times 12$  MHz and coupling strength of  $g = 2\pi \times 15$  MHz.

photon is emitted from the cavity mode, leaving the system in  $|g, 0\rangle$ , decoupled from further evolution. Atoms are loaded into the cavity with an atomic fountain, from a magneto-optic trap (MOT) located directly under the cavity.

The spatio-temporal profile  $\zeta(t)$  of the emitted photons can be directly controlled by shaping the driving pulse [16] using an acousto-optic modulator (AOM). For our purposes, it is most crucial that the phase of the driving laser, which we control via a separate electro-optic modulator (EOM), is directly mapped to the phase of the emitted photon. Fig. 2(b) shows the driving pulse shape and Fig. 2(c) the resulting doubly-humped photon profile, evenly distributed across two 225 ns time-bins, for a total coherence time of  $\delta t = 450$  ns.

The experimental sequence for the production of photons is as follows: photons are emitted at a repetition rate of 1 MHz, with 450 ns of the cycle used for the production of a single photon. The remaining 550 ns of the cycle are used to optically repump the atom to  $|e\rangle$  to repeat the process. The photons impinge on a polarising beam splitter (PBS), and are randomly routed into two paths, one of which incorporates a fibre loop of 300 m of optical path length to induce a  $1 \mu\text{s}$  delay. This ensures that a pair of subsequently emitted photons arrives simultaneously at the beam splitter, which is the only case of interest. A half wave plate (HWP) sets the relative polarisation of both photons.

Note from Fig. 2(c), that the first halves of the emitted photons span 67.5 ns ( $\sim 225$  ns), despite the optical path length between the cavity and the detectors being only 1.5 m or 301.5 m, depending on the path taken. This means that the first time interval of the two photon state is already being measured before the second half of the second photon leaving the cavity (travelling along the

shorter path) has been fully generated. The length of the interfering photons is sufficient for a feedback loop to alter the phase  $\phi$  of the second half of the photon under production, conditioned on the measurement outcome within the first time interval (Fig. 1.)

The feedback is implemented using a home-built circuit controller and single photon counting modules (SPCMs) with a quantum efficiency of 60-65% and a resolution of  $< 300$  ps (Excelitas SPCM-AQRH-780-14-FC). The total feedback loop latency, from the EOM via the cavity to the SPCM, then back to the EOM via the controller circuitry is  $97.0 \pm 0.2$  ns. Therefore, a conditioned phase change cannot be realised in time if a photon detection in  $I_2$  occurs less than 97 ns after a detection in  $I_1$ . The resulting error rate is limited to 0.2% for a  $\sin^4(t)$  photon intensity envelope. All photon counts are recorded with 81ps accuracy using a qutools quTAU time-to-digital converter (TDC). Detections within the 450 ns photon window are further processed for a dark count correction for each SPCM. A detailed description on the error rates, time budgets, the implementation of the logical feedback circuit and background correction is provided in the Supplemental Material.

#### IV. RESULTS

There are two different ways to look at the measured data. One has been discussed previously and corresponds to Fig. 3, which shows the coincidence probability as a function of the time-difference between two detections. However, our main interest is whether both detections are registered within the same or opposite time intervals ( $I_1$  and  $I_2$ ). Therefore, the same data can be represented in a cross-correlation diagram (Fig. 4) showing the four possible values of the coincidence probability between detectors  $C$  and  $D$  firing in either  $I_1$  or  $I_2$ . In contrast to Fig. 3, this allows to further differentiate between coinciding detections in  $I_1$  and  $I_2$ .

The cross detection probability of interfering photons with perpendicular polarisations is shown in Fig. 3(a). This gives rise to the random routing of the simultaneously arriving photons, such that the resulting time-resolved coincidence rate yields the autocorrelation function of the photons' intensity profile. The cross-correlations are depicted in Fig. 4(a). For the case of photons with orthogonal polarisations, these are identical and theoretically equal to  $1/8$ .

For photons with parallel polarisations, the cross correlation probability is shown in Fig. 3(b) for  $\phi = 0$ . This measurement follows the predictions of photon bunching in the canonical HOM effect, for which we expect no coincidences. Photons bunch in the same output regardless of the actual detection time. Thus, the probability of cross channel detections is expected to be zero for all time differences (Fig. 4(b)).

Fig. 3(c) shows the cross detection probability for photons with parallel polarisations when  $\phi = \pi$ . In this case, the photons antibunch (i.e., they are found in different output channels if detected in different time intervals). The maximum probability to find photon-photon correlations occurs at  $\tau = \pm\delta t$ , where  $\delta t$  is the length of the photons. This maximum probability is twice the reference value of Fig. 3(a), which is in accordance with the cross-channel detections shown in Fig 4(c). Nonetheless, the likelihood of correlated photon detections in the same time interval is close to its theoretical value of zero.

Finally, the cross detection probability shown in Fig. 3(d) represents the case of active feedback on  $\phi$ , for which we expect any photon recorded in  $I_2$  be detected at  $C$ . Therefore, the number of " $D$  before  $C$ " correlations reaches a maximum while we barely see any " $C$  before  $D$ " correlations, as shown in Fig. 4(d). Our experimental results demonstrate that classical feedback control of a quantum excitation spanning multiple systems (RF pulse driving AOM  $\rightarrow$  driving laser  $\rightarrow$  atom  $\rightarrow$  cavity  $\rightarrow$  quantum field modes) can be achieved, resulting in a photonic state with the property of always exiting through the same output of a beam splitter.

Some differences between theoretical expectations and experimental results are visible in Figs. 3 and 4. These can be attributed to a partial loss of coherence or depolarisation of the interfering photons, most evident from the presence of correlations in the side lobes of Fig. 3 (b). The mutual coherence between photons is often characterised by the HOM visibility, defined as

$$V_{\text{HOM}} = 1 - \frac{N_{\parallel}}{N_{\perp}} \quad (14)$$

where  $N_{\parallel}$  and  $N_{\perp}$  are the total number of correlations observed for interfering photons with parallel and perpendicular polarisations, respectively. Using the results obtained with  $\phi = 0$  for  $N_{\parallel}$  we find  $V_{\text{HOM}} = 0.78 \pm 0.04$ . However, we measure a reduced visibility of  $V_{\text{ref}} = 0.61 \pm 0.04$  if we restrict our analysis to those correlations with detections across time intervals  $I_1$  and  $I_2$ . This serves as a reference for all effects discussed here, as these affect only the correlations across both time intervals.

The visibility under phase control upon switching between  $\phi = 0$  and  $\phi = \pi$  reads

$$V_{\phi} = \frac{N_{\pi} - N_0}{N_{\pi} + N_0}, \quad (15)$$

where  $N_0$  and  $N_{\pi}$  represent the coincidence counts between pairs of photons with relative phase shifts of  $\phi = 0$  and  $\pi$ , respectively. Again, we only count coincidences across  $I_1$  and  $I_2$ , and find  $V_{\phi} = 0.56 \pm 0.06$ , in agreement with  $V_{\text{ref}}$  within error bars. This validates the robustness of the phase switch as no further loss of coherence

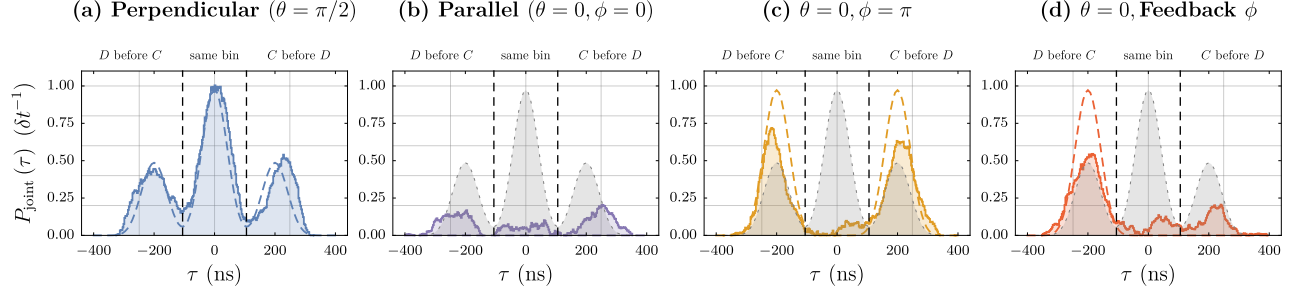


FIG. 3: Coincidence probability densities and sliding histograms (whose bin width is larger than its bin separation) showing the theoretical (dashed) and experimental (solid) values for  $P_{\text{joint}}(\tau)$ . This illustrates the time-resolved HOM interference of two photons under three different conditions. (a) shows the random routing of photons with perpendicular polarisations, which serves as reference. (b) shows the interference between indistinguishable photons ( $\phi = 0$ ) with parallel polarisations, resulting in almost no coincidences between the two detectors. (c) shows the trace obtained for photons with phase shifts of  $\phi = \pi$  without feedback. (d) shows the asymmetric pattern observed under feedback control, where the feedback has prevented (most) correlations in the right satellite peak, steering the second photon to a pre-defined output. This ensures that the cat is always observed alive. The data shown here has been corrected for correlations involving background noise, as explained in the Supplemental Material.

is induced<sup>1</sup>.

Since the feedback relies on a conditional phase switch, we quantify its visibility by comparing coincidence counts between intervals where a measurement in  $D$  occurs before one in  $C$  ( $N_{D1C2}$ ), and vice-versa ( $N_{C1D2}$ ):

$$V_{\text{feed}} = \frac{N_{D1C2} - N_{C1D2}}{N_{D1C2} + N_{C1D2}}. \quad (16)$$

For our experiment, we find  $V_{\text{feed}} = 0.56 \pm 0.06$ , which is identical to  $V_{\phi}$  and equally within error bars of  $V_{\text{ref}}$ . We therefore conclude that the feedback works as expected, without introducing any loss of coherence.

## V. CONCLUSIONS

We have demonstrated a technique for steering the measurement of a quantum superposition towards a definitive result, a result which can be interpreted as ensuring that Schrödinger's cat is always observed alive. This was achieved by using a feedback mechanism that enforces either bosonic or fermionic behaviour on interfering photons with long coherence lengths.

We emphasize that a classical interpretation of the described experiment fails. Classically, one might expect the feedback control to be successful only when the first detection corresponds to the photon in the delay arm. Otherwise, if the first detection was of the photon in the

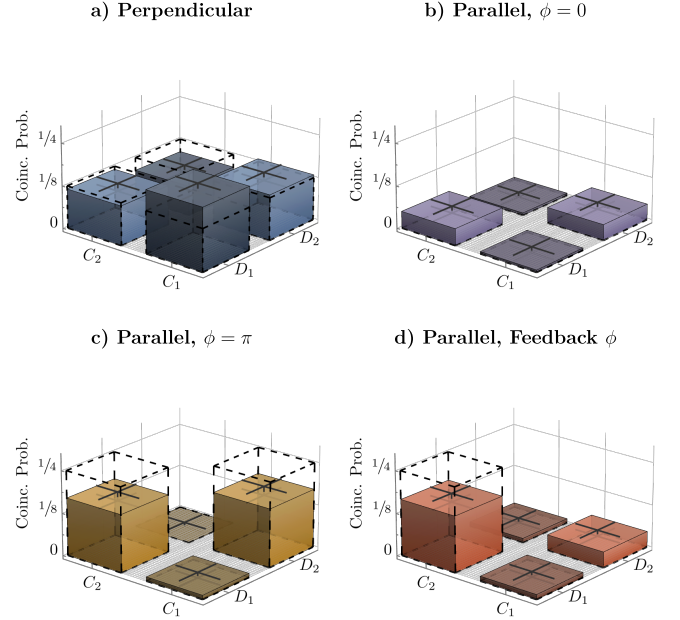


FIG. 4: The correlations from Fig. 3 are now shown according to the exact detector-time-bin detections. In (a), an increased number in the correlations between  $C_1$  and  $D_1$  with respect to  $C_2$  and  $D_2$  is explained due to a larger number of photons in the first time bin, as shown in the Supplementary Material. In (d), we observe an increase in the correlations between  $C_2$  and  $D_1$  with respect to (a). This implies that a detection in  $D$  in  $I_1$  has been used to steer the measurement of a photon in  $I_2$  to  $C$ , and serves as a demonstration that the second photon is sent to a pre-defined output state, i.e., the cat is always observed alive. A limitation in visibility is evident when comparing the data to their theoretical values, shown dashed. The data shown here has been corrected for correlations involving background noise, as explained in the Supplementary Material.

<sup>1</sup>  $V_{\text{ref}}$  and  $V_{\phi}$  are expected to yield the same value, assuming  $N_{\parallel} = N_0$  and  $N_{\perp} = (N_0 + N_{\pi})/2$  due to the random splitting of photons.

short arm, the phase change of the driving laser would have no effect (as the photon under generation has already been detected). In a classical description, one would expect a random routing of the second photon regardless of the phase switch, and a reduction of the feedback visibility to zero, which is clearly not the case.

This result constitutes an elementary step towards introducing active control into processes such as quantum random walks and optical networks [18]. Generalisations of the technique demonstrated here are suitable candidates in photonic switchyards requiring multiple photon streams for studying multi-mode interferometry [19], where the deterministic routing of photons would be performed using feedback operations.

### Acknowledgements

J.R.A. acknowledges Alejandra Valencia, David Guzmán and Sebastián Murgueitio Ramírez for useful discussions.

We dedicate this paper to the memory of Bruce W. Shore, who sadly passed away on 9 January 2021. Bruce inspired us to keep questioning the fundamental principles of the light-matter interaction, and without his deep insight, laid out convincingly in his memoir on our changing views of photons [20], we would never have accomplished the present work.

### Funding

European Union Horizon 2020 (Marie Skłodowska-Curie 765075-LIMQUET).  
EPSRC through the quantum technologies programme (NQIT hub, EP/M013243/1).

- 
- [1] E. Schrödinger, *Naturwissenschaften* **23**, 807 (1935), ISSN 1432-1904.
  - [2] E. Adlam, *Foundations of Quantum Mechanics*, Elements in the Philosophy of Physics (Cambridge University Press, 2021).

- [3] K. Landsman, in *Foundations of Quantum Theory: From Classical Concepts to Operator Algebras*, edited by K. Landsman (Springer International Publishing, Cham, 2017), *Fundamental Theories of Physics*, pp. 435–457, ISBN 978-3-319-51777-3.
- [4] S. Lloyd, arXiv:quant-ph/9703042 (1997), quant-ph/9703042.
- [5] J. Zhang, Y.-x. Liu, R.-B. Wu, K. Jacobs, and F. Nori, *Physics Reports* **679**, 1 (2017), ISSN 0370-1573.
- [6] S. Habib, K. Jacobs, and H. Mabuchi, p. 10 (2002).
- [7] Y. Yamamoto, N. Imoto, and S. Machida, *Physical Review A* **33**, 3243 (1986), ISSN 0556-2791.
- [8] M. A. Armen, J. K. Au, J. K. Stockton, A. C. Doherty, and H. Mabuchi, *Physical Review Letters* **89** (2002).
- [9] W. P. Smith, J. E. Reiner, L. A. Orozco, S. Kuhr, and H. M. Wiseman, *Physical Review Letters* **89** (2002).
- [10] C. Sayrin, I. Dotsenko, X. Zhou, B. Peaudecerf, T. Rybarczyk, S. Gleyzes, P. Rouchon, M. Mirrahimi, H. Amini, M. Brune, et al., *Nature* **477**, 73 (2011).
- [11] X. Zhou, I. Dotsenko, B. Peaudecerf, T. Rybarczyk, C. Sayrin, S. Gleyzes, J. M. Raimond, M. Brune, and S. Haroche, *Physical Review Letters* **108** (2012).
- [12] T. Legero, T. Wilk, A. Kuhn, and G. Rempe, *Applied Physics B: Lasers and Optics* **77**, 797 (2003), quant-ph/0308024.
- [13] T. Legero, T. Wilk, A. Kuhn, and G. Rempe, *Advances In Atomic, Molecular, and Optical Physics* **53**, 253 (2006).
- [14] C. K. Hong, Z. Y. Ou, and L. Mandel, *Phys. Rev. Lett.* **59**, 2044 (1987).
- [15] A. Kuhn and D. Ljunggren†, *Contemporary Physics* **51**, 289 (2010), ISSN 0010-7514.
- [16] P. B. R. Nisbet-Jones, J. Dilley, D. Ljunggren, and A. Kuhn, *New Journal of Physics* **13**, 103036 (2011), ISSN 1367-2630.
- [17] G. S. Vasilev, D. Ljunggren, and A. Kuhn, *New J. Phys.* **12**, 063024 (2010), ISSN 1367-2630.
- [18] A. Peruzzo, M. Lobino, J. C. F. Matthews, N. Matsuda, A. Politi, K. Poulios, X.-Q. Zhou, Y. Lahini, N. Ismail, K. Worhoff, et al., *Science* **329**, 1500 (2010).
- [19] T. D. Barrett, A. Rubenok, D. Stuart, O. Barter, A. Holczek, J. Dilley, P. B. R. Nisbet-Jones, K. Poulios, G. D. Marshall, J. L. O’Brien, et al., *Quantum Science and Technology* **4**, 025008 (2019), ISSN 2058-9565.
- [20] B. W. Shore, *Our Changing Views of Photons: A Tutorial Memoir* (Oxford University Press, New York, 2020), 1st ed., ISBN 978-0-19-886285-7.



# Supplementary material: How to administer an antidote to Schrödinger's cat

## I. SAME-DETECTOR PROBABILITIES

Fig. 3 in the main text shows the subset of probabilities when we only look at cross-detector correlations. For this reason, the value  $\int P_{\text{joint}}(\tau) d\tau$  is bounded by  $1/2$ . A prediction of the theoretical curves for same-detector correlations, given by  $P_{\text{same}}(\tau)$  can be shown in Fig. S1. Given the different possibilities that can arise from photon routing, the normalization for the joint detection probability is given by

$$\int (P_{\text{joint}}(\tau) + P_{\text{same}}(\tau)) d\tau = 1 \quad (\text{S1})$$

## II. LATENCY OF FEEDBACK

To ensure adequate feedback, it is crucial to perform a timely change on the phase  $\phi$ , conditional on detections only in the first time bin. However, not every detection of the SPCM can be used to change the phase of the photon: the latency between the SPCM click and the effect of the feedback electronics can affect the production of a proper photonic state which can be used for feedback. The photon signal takes around 75 ns to reach the output of the SPCMs from the EOM (as seen in the sum of the first two columns of Table S1), during which there is no possibility of achieving feedback control.

The probability of a correlation (with one detection in each time bin) occurring during the dead time is given by

$$P(\tilde{t}) = \int_{\max[\frac{1}{2}-\tilde{t}, 0]\delta t}^{\frac{1}{2}} f(t_1) \int_{\frac{1}{2}}^{\min[t_1+\tilde{t}, 1]\delta t} f(t_2) dt_2 dt_1 \quad (\text{S2})$$

where  $\tilde{t}$  is the dead time given as a fraction of the total photon length  $\delta t$ ,  $t_1 \in (0, \frac{1}{2})\delta t$  and  $t_2 \in (\frac{1}{2}, 1)\delta t$ , and

$$f(t) = \frac{16}{3} \sin^4(2\pi t/\delta t) \quad (\text{S3})$$

is the intensity envelope of the produced photons.

The error rate remains negligibly small for dead times of up to around a fifth of the total photon length before increasing rapidly, as shown in Fig. S2. In our experiment, the control and effecting stages are implemented in 13ns, resulting in a total latency for the feedback of 97ns, corresponding to an expected error rate of 0.2%. Table S1 details the latency breakdown.

Element	Time (ns)
Optical Transit Time EOM $\rightarrow$ Cavity $\rightarrow$ SPCM	45
SPCM Response	35
Circuit Response	7.0
Signal Rise Time	5.5
Total Cable Delay SPCM $\rightarrow$ Control $\rightarrow$ EOM	4.5
Total	97.0

TABLE S1: A breakdown of the contributing elements to the feedback delay. The first two rows are not known absolutely, only their sum was measured. From discussions with the manufacturer it is believed that the SPCM response (time delay between photon impact and TTL output) is around 35 ns.

## III. FAST ELECTRONICS

The task of the feedback controller is to decide whether or not a phase should be applied to the second time bin and, if so, quickly supply sufficient voltage to the electro-optic modulator to enact that phase change. To that end, a custom in-house circuit was built using off the shelf transistor-transistor logic (TTL) integrated circuit (IC) logic chips. The circuit toggles between one mode of operation with no effect and another one which ensures a phase change to the EOM during the second time bin. An abbreviated circuit logic diagram outlining the functioning of the circuit is shown in Figure S3. The control circuit receives as inputs a copy of the TTL output from the SPCM of interest, **det**, and two 215 ns TTL window pulses from the AWG,  $W_{\text{det}}$  and  $W_{\text{phase}}$ , which respectively outline the first time bin for the registering of detections and the second time bin for the output phase voltage, **phase**.

## IV. DATA PROCESSING

The data recorded by the SPCMs is processed to yield the sliding histograms and bar charts shown in Figures 3 and 4. This data contains a significant amount of noise coming from detector dark counts and other stray photons, which need to be corrected for. Five procedures are performed in the raw data after clicks are recorded in detectors  $C$  and  $D$ :

**A. Gating the raw data:** Correlations need to be found between the raw data. The time scale is cropped to account for photon arrival times and repumping times, which are eliminated accordingly from the scale. This is shown in Fig. S4 (a).



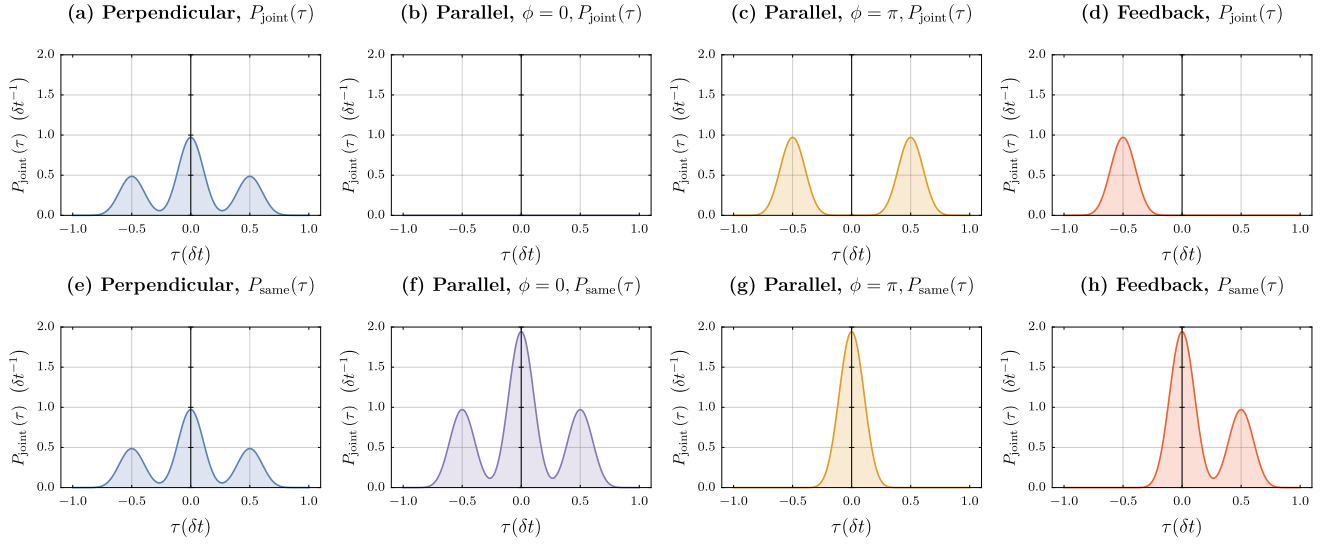


FIG. S1: Theoretical curves for  $P_{\text{joint}}(\tau)$  for cross-detector (a-d) and same-detector coincidences (e-h), for the same cases described in Fig. 3 from the paper. Subfigure (f) shows that, when photons are identical, all the detections happen in the same detector, albeit possibly in different time bins. Once more,  $\delta t$  corresponds to the length of the single photons.

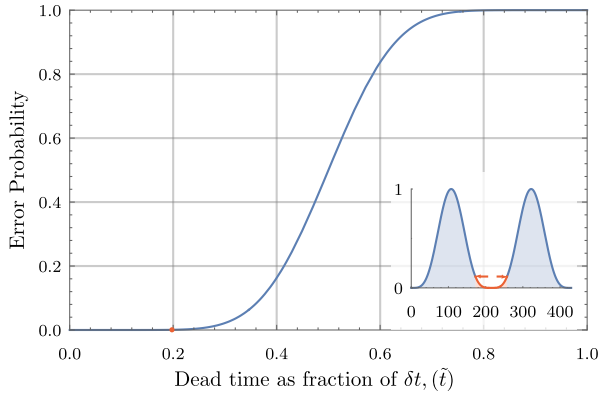


FIG. S2: Feedback error analysis: The dead time is the feedback delay of the system, here shown as a fraction of the photon length. Specifically it is the round trip time for a signal to pass from the EOM, via the cavity to the SPCMs, be processed by the controller and return to the EOM. It represents a period of time during which feedback control cannot be achieved, therefore introducing an error rate (Eq. S2). The profile of the considered photon is shown in the inset along with the measured 97 ns feedback delay of the setup marked in red, the corresponding error rate of 0.2% is coincident with the horizontal axis on this scale.

**B. Fitting and calculation of Signal to Noise Ratio:** Once the raw data has been gated, we fit the following function to the raw data in each detector:

$$g(t) = a + \begin{cases} b \sin^2\left(\frac{2\pi(x-p_1)}{p_2-p_1}\right) & \text{for } p_1 < x < p_2 \\ c & \text{for } p_3 < x < p_4 \end{cases} \quad (\text{S4})$$

Here,  $p_1$  and  $p_2$  encompass the times for photon

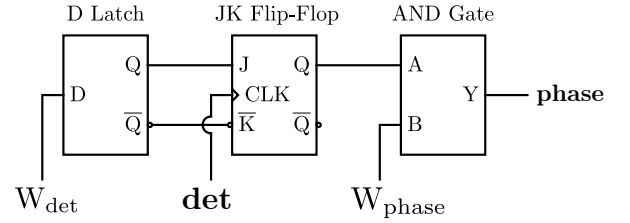


FIG. S3: Control circuit: The JK flip-flop (TI SN74F109N) controls the state of operation of the circuit. When  $Q$  is 0, no Phase signal will be output, but when  $Q$  is 1, the output, phase, follows  $W_{\text{phase}}$ , using a wired AND gate with open collector TTL gates (N74F07N). Toggling between these two states is triggered by a signal on the JK flip-flop CLK (clock) input from a detector,  $\text{det}$ , but only when the JK is in toggle mode. With  $Q(\overline{Q})$  high (low) the JK is in toggle mode, with  $Q(\overline{Q})$  low (high) the JK is in Hold mode. The D latch (TI SN74LS375N) buffers the input  $W_{\text{det}}$  to provide a duplicated and negated copy necessary for the JK.

arrivals, while  $p_3$  and  $p_4$  correspond to times when the repumping is triggered. The time between  $p_2$  and  $p_3$  is used to obtain the dark count rates of the single photon counting modules. This fitting is shown in Fig. S4 (b).

**C. Background estimation:** A model for calculating the background is created by using the photon count and dark count rates of the single photon detectors. These rates lead to two distributions for each detector describing the detection events due to photons emitted from atoms,  $m_P^{(C/D)}(t)$ , and true background detections uncorrelated to atoms  $m_B^{(C/D)}(t)$ .

These distributions can be combined to give expected correlations between their pairwise combina-

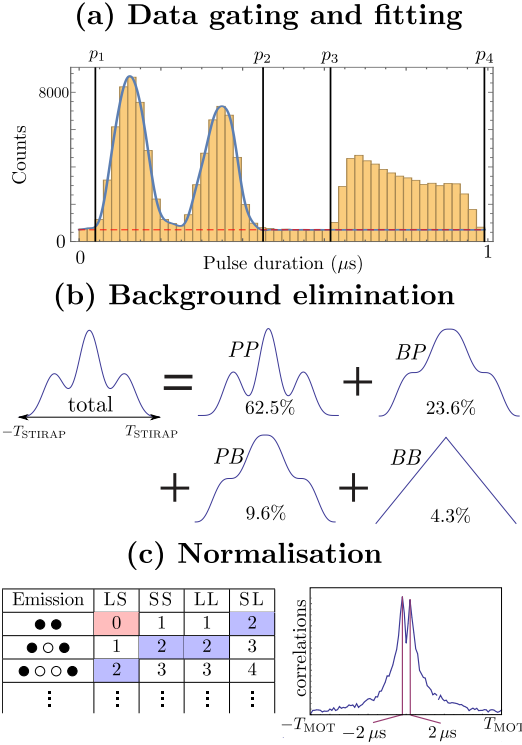


FIG. S4: Background corrections. (a) Shows the photon gating, which fits the photon shape and the repumping following Eq. S4. The photon duration begins in  $p_1$  and ends in  $p_2$ . (b) Shows the four components of the background elimination,  $M_{BB}^{(C)(D)}(\tau)$ ,  $M_{BP}^{(C)(D)}(\tau)$ ,  $M_{PB}^{(C)(D)}(\tau)$  and  $M_{PP}^{(C)(D)}(\tau)$ . (c) shows the normalisation of the correlations. Coincident detections (red), can only occur for a sequential emission of two photons with the first photon entering the delay arm, L and the second entering the short arm S. The normalisation constant is based on the number of correlations at  $\pm 2\mu\text{s}$  in the  $g^{(2)}$  (blue), for which there are four times as many pathways. Correcting for photon losses in the delay arm, we find that the normalisation factor follows Eq. S12.  $T_{\text{MOT}}$  corresponds to the time taken by an atom to be launched from the atomic fountain and fall back again, and the loss in correlations is a direct consequence of the passage of atoms through the cavity.

tions across both detectors:  $M_{BB}^{(C)(D)}(\tau)$ ,  $M_{BP}^{(C)(D)}(\tau)$ ,  $M_{PB}^{(C)(D)}(\tau)$  and  $M_{PP}^{(C)(D)}(\tau)$ , where

$$M_{BP}^{(C)(D)}(\tau) = \int_0^{T_{\text{STIRAP}}} m_B^{(C)}(t) m_P^{(D)}(t + \tau) dt \quad (\text{S5})$$

$$= \left( m_B^{(C)} * m_P^{(D)} \right) (\tau). \quad (\text{S6})$$

and the other terms are defined analogously. The total background is the addition of these terms:

$$M_{\text{total}}^{(C)(D)}(\tau) = M_{BB}^{(C)(D)}(\tau) + M_{BP}^{(C)(D)}(\tau) + M_{PB}^{(C)(D)}(\tau) + M_{PP}^{(C)(D)}(\tau). \quad (\text{S7})$$

Case	Coincidence rate / noise
Fig. 3(a) - Perpendicular	2.02
Fig. 3(b) - Parallel, $\phi = 0$	0.37
Fig. 3(c) - Parallel, $\phi = \pi$	1.40
Fig. 3(d) - Parallel, feedback $\phi$	0.94

TABLE S2: Integrated coincidence rate and integrated noise correction ratio of the different time-resolved HOM histograms. The noise has been eliminated from Fig. 3 in the main text.

The  $M_{PP}^{(C)(D)}$  term accounts for the expected correlation rate between two atoms producing photons by the distribution  $m_P^{(C)(D)}$ , and can be discarded as we are only interested in the correlations of photons within the same emission period. A plot of the four terms composing  $M_{\text{total}}^{(C)(D)}(\tau)$  is shown in Fig. S4 (c). Upon removing  $M_{\text{total}}^{(C)(D)}(\tau)$ , the ratio between the integrated coincidence rate and the integrated noise correction of the different contributions is given by Table S2.

**D. Maximum likelihood estimation of correlation counts:** The total number of observed correlation counts  $O(\tau, \delta\tau)$  between  $\tau$  and  $\tau + \delta\tau$  is equal to

$$O(\tau, \delta\tau) = S(\tau, \delta\tau) + B(\tau, \delta\tau), \quad (\text{S8})$$

i.e. the sum of signal correlation counts  $S(\tau, \delta\tau)$  and background correlation counts  $B(\tau, \delta\tau)$  calculated from  $M_{\text{total}}^{(C)(D)}(\tau)$ . From  $O(\tau, \delta\tau)$ , we can extract the most likely mean number of signal correlation counts within such a bin with a maximum likelihood estimation. Assuming that both  $S(\tau, \delta\tau)$  and  $B(\tau, \delta\tau)$  follow independent Poisson distributions with parameters  $\lambda_S$  and  $\lambda_B$ , respectively, it can be shown that the probability of observing  $n$  counts equals

$$P(O = n) = \frac{e^{-(\lambda_S + \lambda_B)} (\lambda_S + \lambda_B)^n}{n!}, \quad (\text{S9})$$

i.e.  $O(\tau, \delta\tau)$  follows a Poisson distribution with a mean of  $\lambda_O = \lambda_S + \lambda_B$ . Given an observation  $n$  for  $O$  and known  $\lambda_B$  (mean background), the likelihood function for the parameter  $\lambda_S \in [0, \infty)$  is given by

$$\mathcal{L}(\lambda_S | n, \lambda_B) = P_{\lambda_S}(O = n), \quad (\text{S10})$$

which is maximised for the intuitive value of

$$\lambda_S = \max\{0, n - \lambda_B\}, \quad (\text{S11})$$

i.e. the number of observed counts minus the background, constrained to a positive number.

**E. Normalisation:** Due to experimental errors in detectors, such as losses and dead times, it is not possible to identify directly how many individual photon-pair experiments were performed by counting the number of detection events measured in one detector. To

overcome this, it is possible to notice that the number of events happening simultaneous is related to the number of events happening separated by two duty cycles, following the relation

$$N_0/N_2 = \frac{\eta_L}{1 + 2\eta_L + \eta_L^2} \simeq 1/4, \quad (\text{S12})$$

where  $\eta_L$  is the probability of photon transmission in the fibre delay.